Spin-dependent optical charge transfer in magnetite from transmitting optical magnetic circular dichroism

Jiunn Chen,* Hua-Shu Hsu, and Ya-Huei Huang
Department of Applied Physics, National Pingtung University, Pingtung 90003, Taiwan

Di-Jing Huang
National Synchrotron Radiation Research Center, Hsinchu 30077, Taiwan

(Received 9 April 2018; revised manuscript received 28 June 2018; published 24 August 2018)

In this study, we demonstrate that optical magnetic circular dichroism (OMCD) in Faraday geometry can serve as an effective means of characterizing the valence electronic structure of magnetic oxide systems. Molecular-beam-epitaxy-grown magnetite thin film single crystals served as the test sample. The dominant spin channels of optical charge transfer were resolved from transmitting OMCD spectra, which can only be interpreted by considering electron correlation effects and including polarized $2p$ oxygen. First-principles calculations based on density-functional theory with Hubbard-U correction (DFT+U) were performed on cubic inverse spinel Fe_3O_4 ($Fd\bar{3}m$). We determined that the main features of optical conductivity [S. K. Park *et al.*, Phys. Rev. B **58**, 3717 (1998)] were similar to those of a Mott-Hubbard insulator. According to the extent of $2p$ character in the mixed Fe($3d$)-O($2p$) valence that engendered the relaxation of Laporte selection, we classified dominant optical charge transfer into three categories: (1) intervalence spin-minority $d-d$ charge transfer relax from lattice distortion; (2) intersublattice $d-d$ charge transfer across the valence gap of spin majority; and (3) ligand-to-metal $p-d$ charge transfer across the valence gap of spin minority. We conclude that the transmitting OMCD spectrum can generally reflect the competition between optical transitions from the B-site Fe($3d$) spin majority and the O($2p$) spin minority. Finally, we found the OMCD signal of magnetite exhibited similar trend to the valence band spin polarization deduced from Mott spin polarimetry. Excitation spectrum that access the direct information about the "bare" electronic states from soft x-ray spin-resolved photoemission were also revisited.

DOI: 10.1103/PhysRevB.98.085141

I. INTRODUCTION

The development of flexible and efficient magnetic characterization techniques is an urgent research priority especially for demanding applications based on thin film/nanocomposite heterostructures, such as spin-dependent transport devices and contrast media for magnetic resonance imaging. Table-top optical probes are integral to studies on the origin of spin-dependent charge transfer. The use of optical magnetic circular dichroism in Faraday geometry (OMCD) providing direct access to spin-spit interband transitions is considered to be more beneficial for efficient in-line characterization, compared with the use of soft x-ray MCD. Transmitting OMCD can be used to determine the absorptive difference between spin channels to resolve the polarized valence states involved. This technique has been successfully demonstrated to be sensitive to polarized electronic states near the band edge [1,2]. Gehring *et al.* [3] provided a comprehensive review of the transmitting-OMCD measurement on Co-doped ZnO, and $GdMnO_3$ thin films deposited a transparent substrate. Studies have also probed the magnetic properties of Fe_3O_4 containing nanoparticles [4–6]. Spinel ferrites with dispersed spin, charge, and lattice degrees of freedom within the entire valence are particularly suitable for the further testing. For Fe_3O_4, a model system of correlated magnetic oxide, direct interpretation of the transmitting OMCD spectrum is far from trivial. Substantial investigation into electron-correlation effects on optical absorption is essential.

Well-ordered crystalline thin films provide accurate atomic arrangements for spectroscopy measurement. Magnetite thin film single crystal involving different sublattice and spin states of iron is particularly desirable for the test. Magnetite has been one of the most intensively studied oxides [7,8]. Fontijn and Zaag [9–11] performed several pioneering studies on polar Kerr ellipsometry to determine the stoichiometry and magneto-optical properties of magnetite in bulk and thin-film form, and the scholars were especially successful in determining the crystal-field transition [12,13].

Fe_3O_4 crystalizes in an inverse spinel structure; in this structure one third of the Fe ions are tetrahedrally surrounded by four oxygen atoms and the remaining two thirds are octahedrally surrounded by six oxygen atoms, denoted as A and B sites, respectively. Electronic states are mainly threefold t_{2g} and twofolds e_g from crystal field splitting. Exchange interaction causes the high-spin configurations, as shown in Fig. 1, that the Fe^{3+} of A and B sites can be represented by $e_g^{2\downarrow}t_{2g}^{3\downarrow}$, and $t_{2g}^{3\uparrow}\,e_g^{2\uparrow}$, respectively, and Fe^{2+} of the B site can be represented by $t_{2g}^{3\uparrow}\,e_g^{2\uparrow}\,t_{2g}^{\downarrow}$. Fe_3O_4 is a ferrimagnet in which the magnetic moments of the Fe ions at each site are antiparallel coupled below a temperature of approximately 860 K. Hereafter, majority/minority electrons refers to electrons whose spin directions are parallel/antiparallel to the net magnetization.

*Corresponding author: asesrrc@gmail.com

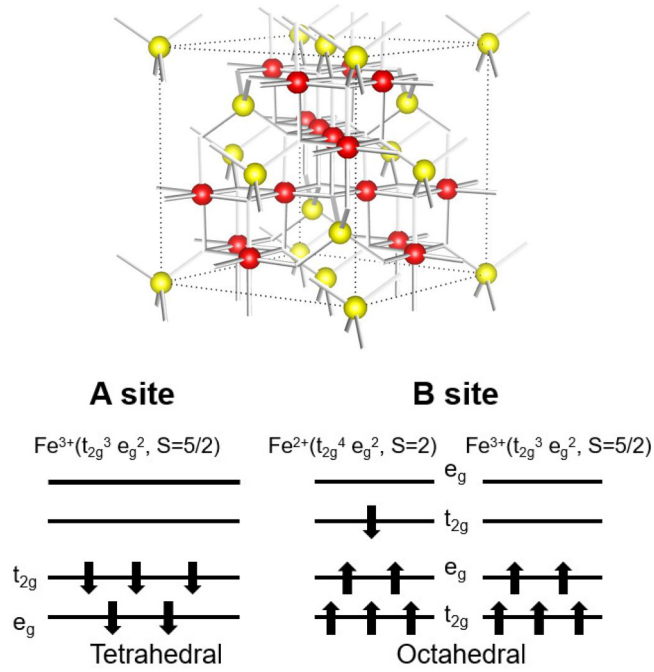

FIG. 1. (Top) Crystal structure of Fe_3O_4 in the [110] direction. Yellow and red balls denote Fe ions at tetrahedral (A) and octahedral (B) sites, respectively. The oxygen ions are not shown here for simplicity. (Bottom) Electronic configuration based on pure ionic picture. A total of 5 and eleven electrons in high-spin configuration were associated with spin moment of 2.5 and 4.5 μ_b, respectively, in each sublattice per unit cell.

Based on a simple ionic picture, the intervalence hopping of B-site $t_{2g}^{\downarrow}$ engenders a finite conductivity at temperatures above approximately 120 K, the Verwey temperature (T_V) [14]. Earlier band descriptions based on density functional theory (DFT) suggested that the half metallicity can be realized above T_V and that the correlation effect of $3d$ electrons stabilizes the long range charge-ordering gap at low temperature [15,16]. Incorporating structural refinement of monoclinic phase in low temperature [17], subsequent DFT + U studies [18–21] indicated not only a charge ordering which is consistent with the experiments but also an associated t_{2g} orbital ordering. The finding of this t_{2g} orbital ordering is evidently supported from resonant soft x-ray diffraction technique in the form of bulk [22] and thin film [23,24]. More recently, Senn, Wright, and Attfield [25] demonstrate that the Verwey transition is due to the ordering network of three-Fe-site distortion termed trimerons, comprising two outer Fe^{3+} ions as acceptors and a central Fe^{2+} ion as a donor. The distortion elongates the four Fe-O bonds in a $Fe^{2+}O_6$ octahedron in the xy plane, removing the degeneracy of the t_{2g} orbit within a trimeron, and creates an energy separation $\Delta_{t_{2g}}$ between d_{xy} and d_{yz}/d_{zx} [18]. The trimeron correlation persists in the cubic phase at temperatures exceeding T_V [26].

Over the past decade, efforts have been devoted to reconciling the origin of the Verwey transition. Electron correlation effects to a larger energy scale that optical absorption involved has not received equal attention. To date, the revealing knowledge is that the t_{2g} electrons are distributed over the B-site Fe ions, rather than fully localized in the form of Fe^{2+} states [25,27,28]. A previous valence band resonant photoemission study [29] also indicated indistinguishable contributions Fe^{2+} and Fe^{3+} emission. Thus, all B-site Fe atoms should be considered equivalent above T_V [30,31]. According to the Zaanen-Sawatzky-Allen (ZSA) classification scheme [32], Fe_3O_4 belongs to Mott-Hubbard insulator in which the charge transfer energy of $p - d$ is higher than that of $d - d$. Therefore including the oxygen $2p$ character as well as electron correlation effects in interpreting the magneto-optical properties of magnetite is practical [33,34].

In this study, the spin-dependent channels of optical charge transfer within magnetite were resolved from transmitting OMCD spectrum. Characteristic features associated with dominant spin channels were mapped, and optical gaps of spin majority and spin minority were determined. Moreover, the OMCD signal of magnetite exhibited a similar trend to the valence band spin polarization deduced from Mott spin polarimetry. Therefore, bare electronic states revealed by soft x-ray spin-polarized photoemission (SPES) were also revisited. The rest of this paper is organized as follows. Section II describes the experimental details including epitaxial film growth and structural characterizations. Electronic structures and optical properties determined on the basis of DFT+U, OMCD, and SPES are presented in Secs. III, IV, V, and VI followed by the conclusion.

II. FILM GROWTH AND CHARACTERIZATIONS

Magnetite thin films were grown on *ex situ* cleaved MgO single crystals by using oxygen-assisted MBE. Both the rock-salt structure of MgO and the inverse spinel structure of Fe_3O_4 are based on an fcc oxygen anion lattice. The lattice constant of Fe_3O_4 (8.396 Å) is approximately twice that of the MgO (4.211 Å), resulting in a small lattice mismatch (∼0.3%). Thus, a MgO single crystal provides an ideal template for the epitaxial growth of Fe_3O_4 thin films and allows the formation of a continuous oxygen sublattice over the MgO/Fe_3O_4 interface [35]. When stable oxides Fe_3O_4 and α-Fe_2O_3 on MgO(100) can be obtained from molecular O_2 oxidizing agent, Voogt *et al.* [36] reported the preparation of epitaxial thin film of all iron oxide phases from NO_2-assisted molecular-beam epitaxy. Stoichiometry determination from their works were based on Mössbauer spectroscopy that is sensitive to the intensity ratio of averaged valence charge states, i.e., $Fe^{2.5+}$ and $Fe^{3.0+}$ in the B and A site, respectively.

Base pressure was approximately 10^{-10} Torr. Substrates were annealed at 650 °C in an oxygen atmosphere of 5×10^{-8} torr for 1 to 2 h to remove contaminants such as hydrocarbons. Fe_3O_4 thin films were grown by evaporating Fe atoms from a water-cooled effusion cell in the presence of a background oxygen pressure of approximately 5×10^{-7} Torr. The MgO(001) substrates were maintained at 250 °C to achieve adequate oxidation during growth. Three diffraction rods as well as parabolic Kikuchi lines of MgO RHEED pattern, as illustrated in Fig. 2(a), were clearly presented, indicating a suitable near-surface three-dimensional 8crystalline order. The periods of RHEED oscillations were recorded on a specular spot while Fe was deposited in the presence of oxygen. The assumption that each oscillation corresponds to the formation of one atomic monolayer (ML), a thickness of 0.21 nm (1/4 of the unit cell height), was adopted. Figure 2(b) shows the RHEED

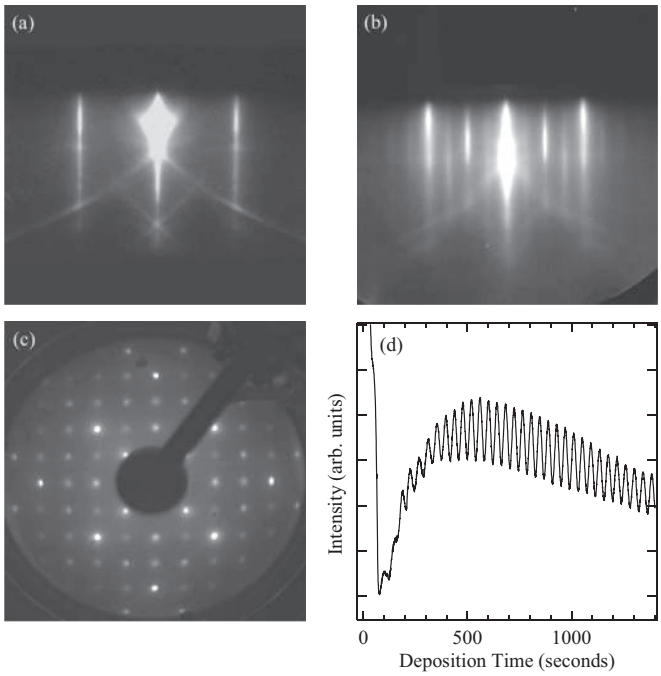

FIG. 2. (a) RHEED pattern from a clean MgO(001) substrate and (b) 100-ML Fe_3O_4/MgO(001) thin film. The incident electron beam is parallel to [100], with a kinetic energy of 15.5 KeV. (c) LEED pattern of Fe_3O_4 thin films determined at a primary energy of 106 eV. (d) Intensity oscillation of the RHEED specular beam during the growth of Fe_3O_4 films.

pattern of grown Fe_3O_4/MgO(001), in which film formation is evidently identified by half-order rods located halfway of the MgO pattern. The quarter-order diffraction rods indicate the twice lattice constant of Fe_3O_4. Surface reconstruction was demonstrated by low-energy electron diffraction (LEED) patterns [Fig. 2(c)]. The spots were doubled along the (110) direction but were determined to be fourfold spots along the (100) direction. The fourfold spots corresponded to the quarter diffraction rod in RHEED with the electron beam incident along the (100) direction. The observed patterns correspond to a $(\sqrt{2} \times \sqrt{2})R45^o$ reconstruction. Notably, that the entire reconstruction was observed as the oxygen pressure varied from 5×10^{-8} to 1×10^{-6} Torr during growth, implying the reconstruction was independent of the stoichiometry. Previous studies have shown that the reconstruction was independent of the oxidizing agent; that is, the reconstruction was observed irrespective of the use of NO_2, molecular O_2, or oxygen plasma [36–41]. "Polar catastrophe"—a sudden electronic reconstruction that compensates for ionic polar discontinuity at the surface or film substrate interface is considered a likely explanation. Chang *et al.* [42] have investigated the initial growth of the Fe_3O_4/MgO(001) interface by using Fe L-edge absorption with thickness variations of 0.67–8 ML, concluding that A sites were completely missing in the first monolayer.

Film crystallinity was characterized through high-resolution x-ray diffraction. Figure 3(a) illustrates the azimuthal scans of the off-normal MgO(111), Fe_3O_4(311), and Fe_3O_4(511) Bragg peaks with respect to the MgO(001) direction. These azimuthal scans are shown to exhibit a fourfold symmetry; the full width at half maximum of the Fe_3O_4(311)

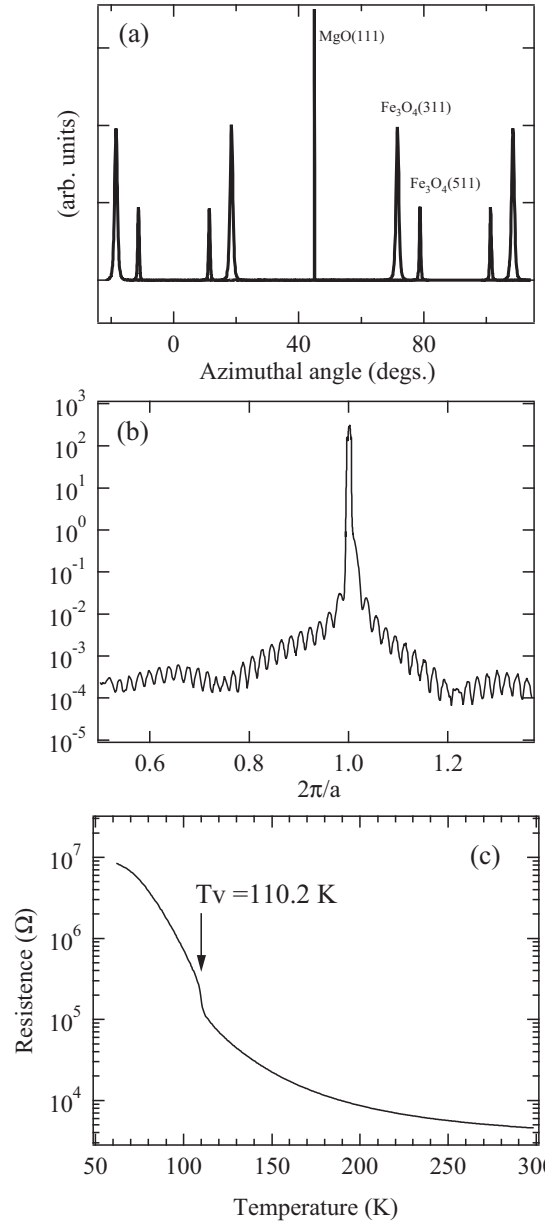

FIG. 3. (a) Azimuthal scans of x-ray diffraction and (b) intensity variation along the off-specular MgO(111) crystal truncation rod. (c) Temperature-dependent resistance of 100-ML magnetite thin film.

and (511) peaks were 1.1° and 0.6°, respectively. The relative positions of these peaks confirmed that the crystallographic axes of the Fe_3O_4 film were well aligned with those of the MgO substrate. Figure 3(b) presents the x-ray reflection along an off-specular MgO(111) crystal truncation rod (CTR). Pronounced interference fringes persisting over a wide range were observed, confirming that the atomic arrangement of the Fe_3O_4 thin films was in good agreement with that of the MgO substrates and that the interfacial roughness was low. A longer intensity modulation period was observed on the CTR, and it was attributed to the MgO capping layer. Overall, the x-ray scattering results confirm that the Fe_3O_4 thin films grown on MgO(001) were epitaxial and of high quality. The lattice parameter of the Fe_3O_4 films along the surface normal was

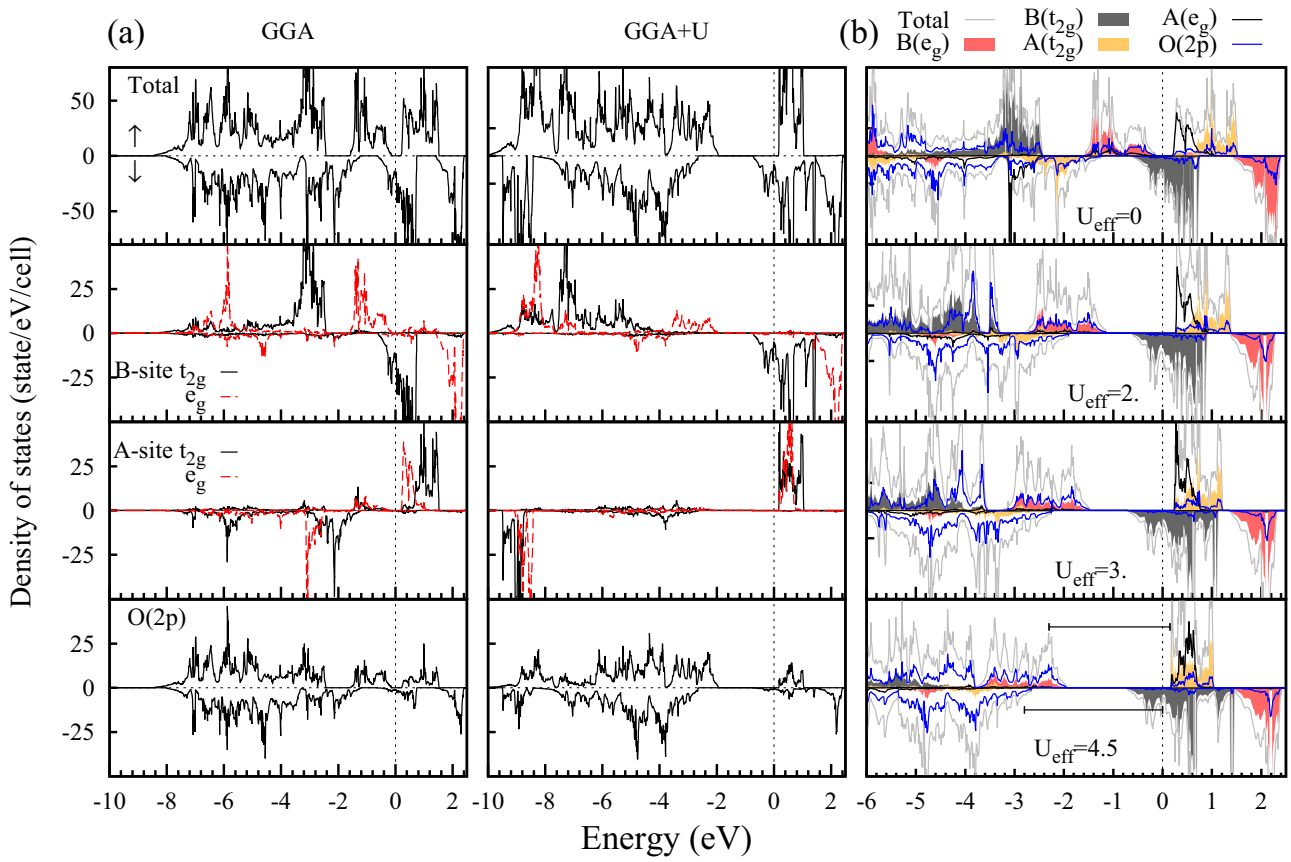

FIG. 4. (a) Total and PDOS results obtained through GGA (left) and GGA+U (right) calculations. Fermi level is indicated by the dashed line through the zero energy. The effective on-site Coulomb energy $U_{\text{eff}} = U - J$ and exchange parameter $J = 0.89$ eV were determined to be 4.5 and 0.89 eV, respectively. (b) PDOS variation with respect to U_{eff}. Valence gap of spin majority involving $B(e_g) \uparrow - A(e_g; t_{2g}) \uparrow$ as well as spin minority involving $O(2p) \downarrow - B(t_{2g}) \downarrow$ are also indicated.

contracted by approximately 0.4%, compared with that parallel to the surface.

Figure 3(c) shows the resistance measurement, revealing a clear drop upon heating through 110.2 K. The transition temperature is smaller than that of a single stoichiometric Fe_3O_4 crystal. Slight stoichiometric deviations in bulk samples have been shown to cause a decrease in T_V. For example, for $Fe_{3-\delta}O_4$, $T_V = 115$ K when $\delta = 1.7 \times 10^{-3}$ and $T_V = 90$ K when $\delta = 1 \times 10^{-2}$ [43,44]. Stoichiometric deviation is associated with Fe^{2+} vacancies on the B site. A film exhibiting decreased T_V might have a small fraction of vacancies, strain [45], and antiphase domain boundaries (APB). APBs due to polarity compensation on the film surface were also reported as a source of anomalous magnetic behavior [46–49] deviate from that of the bulk. The strain in the heterostructure is different to the strain accompanying the structural change of bulk Fe_3O_4 as temperature is lower through T_V. It may be invalid to compare the T_V of epitaxially constrained films to that of bulk $Fe_{3-\delta}O_4$ and then infer stoichiometric deviations. Fontijn *et al.* [10,11] reported the stoichiometry characterization of $Fe_{3-\delta}O_4$, valid against Mössbauer spectroscopy, by using polar Kerr spectra.

III. ELECTRONIC STRUCTURE

First-principle calculations were performed by using DFT within generalized gradient approximation (GGA) [50] as implemented in VASP [51]. The calculations were performed on a cell of 56 atoms arranged in a cubic inverse spinel structure; an experimentally determined lattice constant of $a = 8.39$ Å was used [52], and the internal lattice parameters were not constrained for all cases. We adopted a plane waves energy cutoff of 550 eV, $6 \times 6 \times 6$ meshes by Monkhorst-Pack Brillouin zone k-point sampling, and Perdew-Burke-Ernzerhof parametrization [50] for exchange correlation potential. For GGA+U calculations, the on-site Coulomb energy U of simplified Dudarevs scheme [53] was applied for all Fe ions. The frequency-dependent imaginary part of the dielectric function ϵ_2 was calculated through independent-particle approximation as implemented in VASP. The real part of the dielectric function ϵ_1 was then derived through Kramers-Kronig transformation. The absorption coefficient $\alpha(\omega)$ can be expressed as follows: $\alpha(\omega) = \omega\sqrt{2\sqrt{\epsilon_1^2(\omega) + \epsilon_2^2(\omega)} - 2\epsilon_1(\omega)}$. To facilitate the comparison of the calculations with experimental results, the calculated imaginary part of the dielectric function was broadened.

Figure 4 shows the electronic structure of Fe_3O_4. GGA + U calculations revealed the electronic structure in the vicinity of E_F and binding energy interval of 2–6 eV are illustrated in Fig. 5. The valence structure are mainly t_{2g} and e_g states of hybridized Fe($3d$)-O($2p$) bands. For Fe ions at the B site, the antibonding e_g orbitals were energetically superior to the

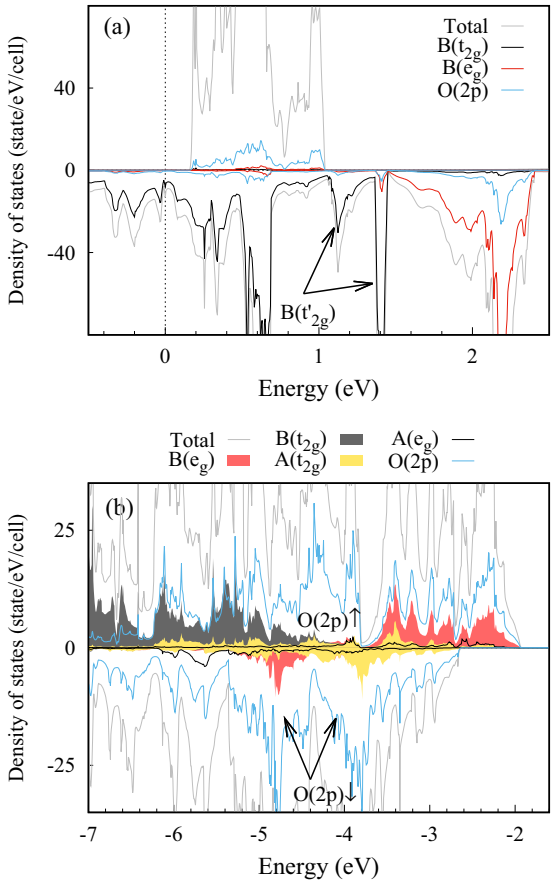

FIG. 5. PDOS derived through GGA + U calculations ($U_{\text{eff}} = U - J = 4.5$ eV, $J = 0.89$ eV) (a) around E_F and (b) 1.5–7 eV below E_F. B-site t'_{2g} minority and polarized $2p$-oxygen are also indicated.

off-axial t_{2g} orbitals. Fe ions at the A site exhibited different symmetries, which engendered opposite signs of crystal field splitting. The GGA+U calculations revealed the same half-metallicity results as the GGA calculations that the off-axial B-site t_{2g} minority [hereafter abbreviated as $B(t_{2g})\downarrow$] across the E_F; these results are consistent with the report of Jeng *et al.* [54] and match the observed t_{2g} band dispersion in the vicinity of the E_F at room temperature [55,56]. We are aware that the correlation gap of charge-ordered states in the cubic phase can be introduced explicitly by intersite interactions at the B site [15] and by a constrained arrangement that reduces $B(t_{2g})\downarrow$ overlapping [57]. Band calculations generally yield the fractional number of d electrons per site that can choose which site to occupy, similar to the case of charge ordering. In this study, we addressed a mixed-valence configuration in addition to the ionic configuration. The deeper energy bands which mixed with O($2p$) were mainly focused for the interpretation of optical charge transfer.

Both GGA and GGA + U calculations revealed that the equilibrium lattice of apical oxygen atoms at the B site slightly deviated from the high-symmetry point. The symmetry was lowered from O_h to D_{3d}. In this case, the trigonal field split the threefold t_{2g} into one single (a_{1g}) and one twofold degenerate (e'_{1g}) levels. The twofold e_g level remained unchanged in contrast to the observation from O_h to D_{4h} [58]. The trigonal

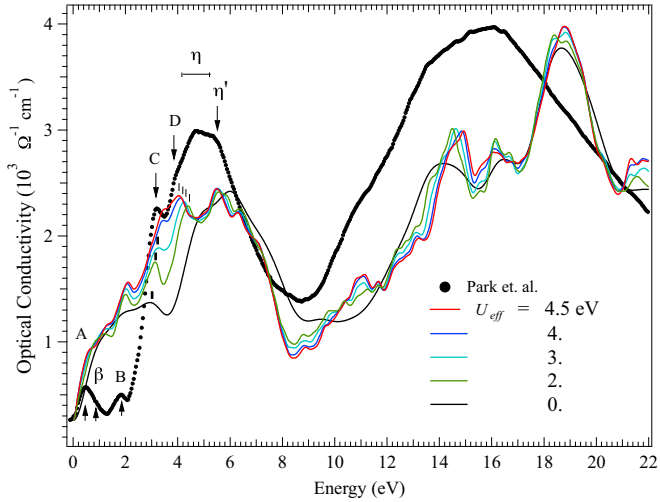

FIG. 6. Calculated absorption coefficient $\alpha(\omega)$ for Fe_3O_4 with various effective on-site Coulomb energy (U_{eff}) compared with experimental data in Ref. [59]. The arrows indicate the main features associated with optical transitions summarized in Table I.

field splitting may be smaller than the bandwidth of $B(t_{2g})\downarrow$, but this symmetry breaking was determined to be crucial for the relaxation of Laporte forbidden.

Regarding the variation between the GGA and GGA + U calculations [Fig. 4(b)], the occupied valence electronic states changed markedly: Increased exchange splitting suppressed $B(e_g)\uparrow$ downward in energy and opens a valence gap of spin majority; U had a relatively low effect on the crystal field splitting at the B site (Δ_o), estimated from the separation of $B(t_{2g})\downarrow$ and $B(e_g)\downarrow$. The minority states at the A-site t_{2g} and e_g [hereafter abbreviated as $A(e_g; t_{2g})\downarrow$] were observed to be pushed to deeper locations below 8 eV. Applying U resulted in the formation of twofold minority $2p$ oxygen [abbreviated as $O(2p)\downarrow$] with a strong $3d$ character in the range of 2.6–5.4 eV, forming a valence gap of spin-minority states connected by the unoccupied $B(t_{2g})\downarrow$. When $U_{\text{eff}} = 4.5$ eV, the valence gaps of the spin-majority and spin-minority states were approximately 2.2 and 2.0 eV, respectively. In addition, rectification of $p-d$ hybridization from Hubbard-U was clearly observed in $B(t_{2g})\uparrow$, from which a polarized $O(2p)\uparrow$ band was removed. When $U_{\text{eff}} = 4.5$ eV, the $O(2p)\uparrow$ band settled between $B(e_g)\uparrow$ and $B(t_{2g})\uparrow$, stabilizing the twofold $O(2p)\downarrow$ state, as illustrated in Fig. 5(b). We thus inferred that electron correlation affected the exchange splitting of the $2p$ oxygen. Moreover, the $B(t_{2g})\downarrow$ that crossed E_F split into two folds with identical symmetry. A state denoted as $B(t'_{2g})\downarrow$ with a narrow bandwidth was lifted to around the middle of $B(t_{2g})\downarrow$ and $B(e_g)\downarrow$ [Fig. 5(a)]. Other unoccupied states included the overlapping $A(e_g)\uparrow$ and $A(t_{2g})\uparrow$ [denoted as $A(e_g; t_{2g})\uparrow$] located immediately above E_F and the axial $B(e_g)\downarrow$ located approximately 2.2 eV above E_F.

IV. OPTICAL TRANSITION

Figure 6 shows the calculated absorption coefficient along with experimental data from Ref. [59]. The features observed within the energy interval 0.5–5.5 eV were the two bumps

within 0.5–2 eV and a predominant absorption peak in the range of 2–6 eV. Experimentally observed features within this energy interval could be interpreted in terms of the direct interband transitions. As depicted in Fig. 5(a), $B(t_{2g})\downarrow$, $B(t'_{2g})\downarrow$, and $B(e_g)\downarrow$ were associated with the possible occurrence of the $d-d$ charge transfer. The lowest lying bump at 0.5 eV (indicated by A) was assigned to the charge transfer within the bandwidth of $B(t_{2g})\downarrow$, which split into two folds because of the lattice distortion. According to the recommendations of Ref. [57], feature A was assigned to $B(a_{1g})\downarrow\longrightarrow B(e'_{1g})\downarrow$. When the possibility of an asymmetric tail (indicated by β) was accounted for, the feature was assigned to $B(t_{2g})\downarrow\longrightarrow B(t'_{2g})\downarrow$, which may be severely suppressed for the limited bandwidth. The bump at approximately 1.8 eV (indicated by B), similar to Refs. [12,60], was assigned to the crystal field transition at the B site [13]. Relative blueshifts of this feature revealed by the calculations may suggest the calculated energy position of $B(e_g)\downarrow$ was excessively higher than the reported value of 1.3–2.0 eV [13,60,61].

We investigated the electronic structure most relevant to optical transition energy exceeding 2 eV [Fig. 5(b)]. The main spin-majority states in this energy interval are outlined as follows: $B(e_g)\uparrow$ in binding energy (BE) range of 2–3.6 eV, $B(t_{2g})\uparrow$ at BE $>$ 4.5 eV, and sandwiched $O(2p)\uparrow$. The corresponding projected density of states (PDOS) suggested that the B-site ions of $B(e_g)\uparrow$ and $B(t_{2g})\uparrow$ were strongly hybridized with O($2p$). $A(t_{2g})\uparrow$ covalency was also found at the deeper end of $B(e_g)\uparrow$ (3.5 eV). The spin-minority states are mainly $O(2p)\downarrow$ with two lobes of strong $3d$ character. The $2p$ character within this interval may relax the parity selection, and this essentially explains the sharp rising edge observed in the interval 2.0–3.1 eV (Fig. 6) of the optical conductivity. As mentioned [Fig. 4(b)], the Hubbard-U enlarged the valence gaps of spin majority and of spin minority, and also separating $O(2p)\uparrow$ from $B(t_{2g})\uparrow$. As increased U, opposite trends of energy separation between $O(2p)\uparrow$ and $B(e_g)\uparrow$ were observed. Thus, the shifting tendencies of states with respect to U may serve as indicators for feature assignment. Therefore, an indicator for assigning the peak at 3.1 eV (indicated by C) was considered to be a blueshift with the increase in U. Accordingly, possible transitions attributed to peak C at approximately 3.2 eV could be the charge transfer across the valence gaps of $B(e_g)\uparrow\longrightarrow A(e_g;t_{2g})\uparrow$ and of $O(2p)\downarrow\longrightarrow B(t_{2g})\downarrow$.

The absorption energy above peak C was mainly characterized by an expanding shoulder D at approximately 3.9 eV. The indicator for assigning this feature was considered to be a redshift with the increase in U. The opposite trends of energy separation observed between $O(2p)\uparrow$ and $B(e_g)\uparrow$ with an increase in U [Fig. 4(b)] may be linked to this feature. Furthermore, a lobe of $O(2p)\downarrow$ in the BE interval 3–4 eV was observed to fall into the same energy range. Therefore, the expanding shoulder D may comprise both $O(2p)\uparrow\longrightarrow A(e_g,t_{2g})\uparrow$ and $O(2p)\downarrow\longrightarrow B(t_{2g})\downarrow$. The preceding assignments were examined further by considering the resolution of dominant spin transitions, as described in the next section.

At a higher absorption energy ($\eta'\sim 5.5$ eV), the successively deeper electronic states in the BE interval 4.5–5.5 eV were involved. As depicted in Fig. 5(b), the $B(t_{2g})\uparrow$ covalent with $O(2p)\uparrow$ and the $O(2p)\downarrow$ both occurred. The recurrence of d character at an absorption energy exceeding 5.5 eV also explains the diminishing intensity beyond η' caused by parity selection. The most intense peak at 4.8 eV (η) could most likely be attributed to feature D and η'. Clearly, Lorentzian broadening in an optical spectrum should increase with the p character. An appropriate broadening function accounting for the degree of $O(2p)$ mixing may reproduce η. However, such a function may impair characteristic features. Additionally, Coulomb interactions between electrons and holes (exciton) are neglected in theoretical calculations.

Optical conductivity of Fe_3O_4 changes most drastically through T_V for energies 0–2 eV (Fig. 2 in Park *et al.* [59]). Our DFT+U applied to the RT phase ($Fd\bar{3}m$) provides the same metallic solution as the DFT, but differs to Leonov *et al.* [21] that have indicated an insulating ground state for the LT phase ($P2/c$). In our case, U with unconstrained condition did not appear to effectively suppress the intensity in 0–2 eV and could not connect to the bandwidth of $B(t_{2g})\downarrow$ at the E_F. Whether the on-site $3d$ Coulomb correction alone is sufficient for describing the pseudogap feature of magnetite above T_V [28,56,62] is debatable. The $d-d$ charge transfer within this region released through vibronic motion may be suppressed due to the intrinsic electron correlation effect of the $2p$ component.

In summary, optical transition of magnetite within the interval 0.5–5 eV mainly indicate the signature of a Mott insulator (the energy of $d-d$ charge transfer is smaller than that of $p-d$ charge transfer). According to the degree of $2p$ character in initial states and the absorptivity, charge transfer can be classified into three types. The first entails $d-d$ charge transfer occurring at 0.5–2 eV and involving $B(t_{2g})\downarrow$ with fewer $2p$ components. Lattice distortion and vibronic coupling are crucial for the relaxation of Laporte selection. The second entails $d-d$ charge transfer mediated by oxygen, which is mainly from $B(e_g)\uparrow$ that hybridized with oxygen. Finally, the third entails ligand-to-metal $p-d$ charge transfer involving states mainly from the $O(2p)$ band. The sharp rising edge observed at 2–3.1 eV in the optical conductivity of magnetite can be considered to represent the conversion of $d-d$ charge transfer into oxygen-mediated $d-d$ charge transfer; that observed at 3.1–3.8 eV can be considered to represent the intermediate range between oxygen-mediated $d-d$ and ligand-to-metal $p-d$ charge transfer that extends to 5.5 eV.

V. OPTICAL MAGNETIC CIRCULAR DICHROISM

This section presents the examination of dominant spin channels accounting for the optical absorption. OMCD in Faraday geometry by using the Jasco J-815 spectrometer were performed on 100-ML epitaxial magnetite thin films. A saturation magnetization of 0.75 T was derived, which was below the magnetic field applied (0.8 T) for the measurement sequence. A 50-kHz photoelastic modulator was switched on to produce both right circularly polarized and left circularly polarized light for measurement. Note that the dependence of the MCD and polarization rotation θ on real and imaginary parts are reversed in the Faraday and Kerr geometries [3]. In Faraday geometry, following Reim and Schoenes [63], MCD and Faraday rotation vary as $-IM(\frac{\delta}{2})=\frac{\omega L}{2c}(k_+-k_-)$

and $\tan\theta = \frac{\omega L}{2c}(n_+ - n_-)$, where $\delta = \frac{2\pi L}{\lambda}(\tilde{n}_+ - \tilde{n}_-)$ represents the phase difference between RCL and LCP. Because the imaginary part of the refractive index relates to the absorption, the absorptive difference from transmitting MCD establishes a direct connection between the magnetically polarized electronic states involved in the optical transition. In addition, the interference from multiple passes has a weaker influence in Faraday geometry and can be prevented with film thickness ($L \sim 20$ nm) an order magnitude smaller than the incident wavelength ($\lambda \sim 500$ nm).

The absorptive differences between spin channels parallel (σ_+) and antiparallel (σ_-) to the net magnetization were recorded simultaneously as a function of wavelength. Different linear optical responses associated with the transitions of spin majority and spin minority were obtained, enabling the determination of the dominant spin transition within certain energy intervals if the spin-flip process could be neglected.

The dominant absorptive spin channel within magnetite can be indicated by the sign of the MCD signal ($\sigma_+ - \sigma_-$). A positive or negative sign corresponds to the dominant spin-majority or spin-minority transition. Figure 7(a) shows the room-temperature OMCD spectrum in the range of 800 – 250 nm. I_+ and I_- denote OMCD spectrum taken with the applied magnetic field in the opposite direction; I_0 denotes the OMCD spectrum at zero field. The contribution of the MgO substrate was not significant in the energy range of interest. The interference effect should also not be interpreted because the obtained signals, I_+ and I_-, were magnetically triggered. The overall OMCD profile revealed general features similar to those obtained for nanoparticles [4,6] and thin films [3], comprising regions of negative MCD signals at the two ends and positive in the middle. To discriminate thermal broadening effects, measurements were conducted at room temperature and at 200 and 25 K. Notably, Verwey transition was not considered for all features of interest, and this is because the energy scale involved varies by hundreds of millielectronvolts through the T_V.

Figure 7(b) shows I_+ as a function of energy, as well as the experimental data (Ref. [59], lower panel) within the same energy interval for comparison. The spectrum can be divided into three regions according to the sign of the MCD signal [$f(E) = \sigma_+ - \sigma_-$]. Region I corresponded to the range of 1.5–2.5 eV with $f(E) < 0$; this region was determined to represent the dominant spin-minority transition. A small bump located near feature B was adequately reproduced for all temperatures and determined to be the crystal field transition of B site. Bump B shifted by approximately 0.2 eV with respect to experimental data, implying the presence of spin-majority transition possibly originating from the surface reconstruction [64,65]. Additional features were the γ (2.35 eV) and δ (2.5 eV), the energy positions of which were at the minimum of Region I and the onset of Region II (2.6–4.4 eV, $f(E) > 0$), respectively. An indicator for the assignment of γ was considered to be the opposite sign of MCD ($f(E) < 0$) and its derivative ($\frac{df(E)}{dE} > 0$), suggesting the occurrence of competitive opposite spin channel at that energy position. Therefore, γ was assigned to optical transition across the valence gap of the spin majority $B(e_g) \uparrow \longrightarrow A(e_g, t_{2g}) \uparrow$. This energy position (2.35 eV) was also compatible with the GGA + U prediction, as indicated in Fig. 4(b). The sign of the derivative changed again ($\frac{df(E)}{dE} < 0$)

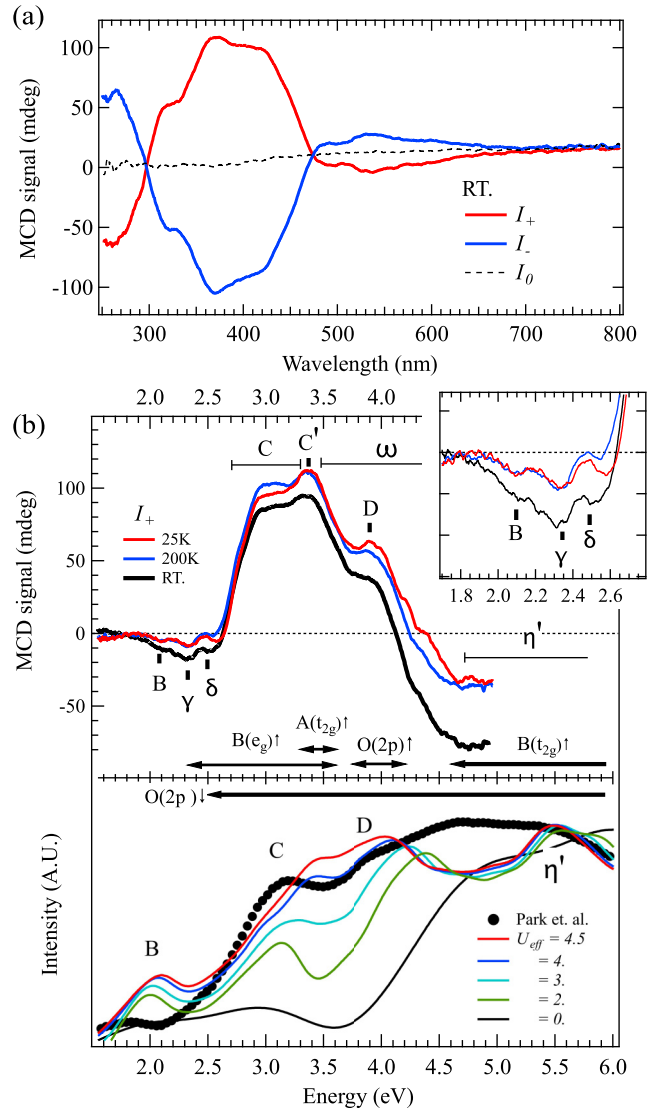

FIG. 7. (a) Room-temperature OMCD spectrum of Fe_3O_4/MgO(100) film. I_0: spectra taken without applied field; I_+ and I_-: spectrum taken with applied magnetic field (0.8 T) parallel and antiparallel to the thickness direction. (b) (Top panel) OMCD spectrum taken at 25 K and 200 K and at room temperature. Letters indicate the optical transition summarized in Table I. Bandwidth and relative band positions are also presented. The inset shows fine structures within 1.8–2.8 eV. (Bottom panel) Theoretical (this work) and experimental (Ref. [59]) absorptive spectra in the energy range 1.5–6 eV.

at approximately 2.5 eV, δ, indicating a reentrant spin-minority transition. We assigned δ to spin-minority transfer across the valence gap of spin-minority $O(2p) \downarrow \longrightarrow B(t_{2g}) \downarrow$. The full participation of the spin-majority transition of $B(e_g) \uparrow \longrightarrow A(e_g, t_{2g}) \uparrow$ was demonstrated by the rising edge (2.65–2.95 eV) of Region II, which peaked in the range of 3.0–3.5 eV. A successive falling edge (ω, 3.5–4.7 eV) was also observed, suggesting occurrence of opposing spin-channel transitions. This was thus assigned to the optical transition of spin minority connected by the lobe of the $O(2p) \downarrow$ band and $B(t_{2g}) \downarrow$. This minority transition actually first occurred at δ.

We observed a bump near feature D located halfway between the falling edge of band ω, with opposite signs of $\frac{df(E)}{dE}$, implying the occurrence of a reentrant spin-majority transition at this energy position. This observation is consistent with the inference in Sec. IV that the expanding shoulder D contains both $O(2p)\uparrow \longrightarrow A(e_g, t_{2g})\uparrow$ and $O(2p)\downarrow \longrightarrow B(t_{2g})\downarrow$ spin channels. According to the analysis presented in Sec. IV, the redshifts [Fig. 7(b) bottom panel] that occurred with increasing U suggested that this feature originated from the polarized $O(2p)\uparrow$ state. In addition, as depicted in Fig. 6(b), a hybridized state $A(t_{2g})\uparrow$ located at a BE of approximately 3.5 eV was observed; moreover, the deeper end of $B(e_g)\uparrow$ was located at approximately 0.4 eV above $O(2p)\uparrow$. This suggests that the peak C' located at the position with the maximum MCD signal relative to feature D can be assigned to both $B(e_g)\uparrow \longrightarrow A(e_g; t_{2g})\uparrow$ and $A(t_{2g})\uparrow \longrightarrow A(e_g; t_{2g})$. Feature C' is immersed in the optical conductivity data. A possible explanation is that the oxygen-mediated charge transfer of $B(e_g)\uparrow \longrightarrow A(e_g; t_{2g})\uparrow$ is impaired by the intrasite charge transfer of $A(t_{2g})\uparrow \longrightarrow A(e_g; t_{2g})\uparrow$.

Table I presents a summary of the dominant transitions along with Ref. [12]. A schematic of the electronic states as well as the optical transition of the features presented in Table I is shown in Fig. 8. In the cubic structure of magnetite, the oxygen and B-site Fe atoms form a network of corner-sharing cubes along the [110] direction (Fig. 1). The corner oxygen atoms of the cubes combine with two Fe ions of the neighboring B site and one Fe ion of the neighboring A site. Apart from the direct $d-d$ charge transfer released from lattice distortion, oxygen atoms intermediated the intersite as well as the intrasite charge transfer through the overlapping $p-d$ orbital states; thus, the Laporte forbidden were relaxed to a larger extent. Therefore, the intervalence charge transfer (IVCT) and the intersublattice charge transfer (ISCT) within magnetite may correspond to the direct $d-d$ charge transfer and the oxygen-mediated $d-d$ charge transfer. According to the leading slope of the three regions of OMCD signal, the dominant optical transitions in magnetite could be classified into three categories: (1) the IVCT of spin minority relax from parity selection due to lattice distortion; (2) the oxygen-mediated ISCT across the optical gap of the spin-majority involving $B(e_g)\uparrow$ that hybridized with oxygen; and (3) the

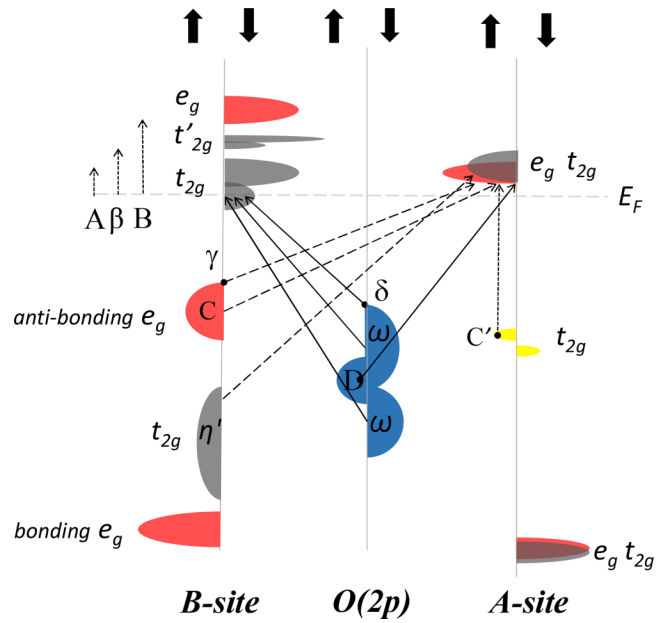

FIG. 8. Schematic of electronic structure of Fe_3O_4 and the associated optical transition within the energy interval 0.5–5.5 eV. Letters indicate the optical transitions summarized in Table I. Intervalence charge transfers (IVCT), intersublattice, and ligand-to-metal charge transfers (ISCT and LMCT) are indicated by dashed, long-dashed, and solid arrow lines, respectively.

TABLE I. Dominant optical transitions in Fe_3O_4 along with Ref. [12]. Assignments from sol-gel synthesized magnetite thin film (Ref. [60]) are also listed for reference. The octahedral and tetrahedral sublattices are denoted by [ ] and (), respectively.

Features	Energy (eV)	Dominant Transition (this work)	CT Type (this work)	Main Transition (Ref. [12])	Main Transition (Ref. [60])
B[a]	2.0	$B(t_{2g})\downarrow \longrightarrow B(e_g)\downarrow$	IVCT	$[Fe^{2+}]t_{2g} \longrightarrow [Fe^{2+}]e_g$	$[Fe^{2+}]t_{2g} \longrightarrow [Fe^{3+}]e_g$
γ[b]	2.35	$B(e_g)\uparrow \longrightarrow A(e_g; t_{2g})\uparrow$	ISCT		
δ[c]	2.5	$O(2p)\downarrow \longrightarrow B(t_{2g})\downarrow$	LMCT		
	2.61			$[Fe^{3+}]e_g \longrightarrow (Fe^{2+})e$	$(Fe^{3+})t_2 \longrightarrow [Fe^{3+}]t_{2g}$
				$(Fe^{3+})t_2 \longrightarrow [Fe^{2+}]t_{2g}$	
C	2.7–3.3	$B(e_g)\uparrow \longrightarrow A(e_g; t_{2g})\uparrow$	ISCT	$[Fe^{2+}]t_{2g} \longrightarrow (Fe^{2+})e$	
C'	3.35	$B(e_g)\uparrow \longrightarrow A(e_g; t_{2g})\uparrow$	ISCT		
		$A(t_{2g})\uparrow \longrightarrow A(e_g; t_{2g})\uparrow$	IVCT		$[Fe^{2+}]t_{2g} \longrightarrow (Fe^{3+})e$
ω	3.5–6.0	$O(2p)\downarrow \longrightarrow B(t_{2g})\downarrow$	LMCT	$[Fe^{3+}]e_g \longrightarrow (Fe^{2+})t_2$	
D	3.9	$O(2p)\uparrow \longrightarrow A(e_g; t_{2g})\uparrow$	LMCT	$[Fe^{2+}]t_{2g} \longrightarrow (Fe^{2+})t_2$	$(Fe^{3+})t_2 \longrightarrow [Fe^{3+}]e_g$
		$O(2p)\downarrow \longrightarrow B(t_{2g})\downarrow$	LMCT	$(Fe^{3+})t_2 \longrightarrow [Fe^{2+}]e_g$	
η'	4.7–6.0	$B(t_{2g})\uparrow \longrightarrow A(e_g; t_{2g})\uparrow$	ISCT		
		$O(2p)\downarrow \longrightarrow B(t_{2g})\downarrow$	LMCT		
η[d]	4.5		ISCT/LMCT	$O_{2p} \longrightarrow [Fe^{2+}]$	

[a]Crystal field transition at B site
[b]Optical gap of spin majority
[c]Optical gap of spin minority
[d]Comprises transitions assigned to feature D and η'

ligand-to-metal $p-d$ charge transfer across the optical gap of the spin minority involving polarized $O(2p)\downarrow$.

Following Fontijn *et al.* [12], feature A is assigned to crystal field transition of magnetite. The optical gap at 2.61 eV is resolved into spin majority (γ at 2.35 eV) and spin minority (δ at 2.5) optical gaps when the resolution of the $p-d$ hybridization and the dominant spin-dependent channels are provided. Feature δ at 2.5 eV was determined to initiate the ligand to metal charge transfer (LMCT) of $O(2p)\downarrow \longrightarrow B(t_{2g})\downarrow$, which was overwhelmed by feature C and returned again as band ω, the falling edge in Region II. Feature D is an important exception engendered by a polarized $O(2p)\uparrow$ state repelling from $B(t_{2g})\downarrow$, which can also be attributed to the electron correlation effect. The transition associated with $B(t_{2g})\uparrow$ can be attributed to the same reason, and this transition occurred only when the absorption energy exceeded 5.5 eV. In addition, the energy positions of the occupied $A(e_g;t_{2g})\downarrow$ states affected by electron correlation were located far beyond the range of interest, except that a minor $A(t_{2g})\uparrow$ component contributed to feature C'.

In short summary, the LMCT dominating the diamagnetic response in magnetite actually initiate at 2.5 eV (δ); the IVST dominating the paramagnetic response initiate earlier at 2.35 eV (γ). The transmitting-OMCD profile generally reflected the optical transition from the B site and demonstrated the competition between spin majority at the B site and spin minority of $2p$ oxygen.

VI. SPIN-POLARIZED PHOTOEMISSION

This section describes the valence band electronic structures obtained from SPES. The experimental details have been provided by previous work [66–69]. The OMCD profile of Fe_3O_4 exhibited a similar trend to the percentage of spin polarization (SP) deduced from Mott polarimetry [70]. Both trends were attributed to the dominant B-site electronic states. Figure 9(a) shows the spin-integrated soft x-ray photoemission spectra taken at room temperature, which resemble those obtained from an *in situ* cleaved bulk sample [62]. The main features of the excitation spectra included a bump around E_F, an expanding shoulder in the range of 0.7–2.9 eV, and main emission peaks in the ranges of 2–4 eV and 6–9 eV. Final state effect obtained from the measurement was attributed to the deeper satellite structure beyond a BE of 10 eV. Figure 9(b) shows the spin-polarized spectrum along with GGA $+U$ calculation results. Figure 9(c) shows the percentage of spin polarization, which can be derived as follows: $SP=\frac{I^+-I^-}{I^++I^-}\times 100\%$, where the I^+ and I^- represent the counts of spin-majority and spin-minority spectrum in Fig. 9(b), respectively. Negative SP in the vicinity of the E_F suggest first ionization dominant by $B(t_{2g})\downarrow$. Spin-majority emission was also observed around E_F, and the SP value at E_F was approximately -40%. Neither bulk-cleaved nor epitaxially grown $Fe_3O_4(001)$ yielded 100% SP around E_F as predicted from band theory [65,68,71–74]. Pentcheva *et al.* [64] suggested the Jahn-Teller stabilization of surface reconstruction engenders the reduction of SP near the emission threshold, as detected from surface-sensitive emission measurements. More recent [55] SPES using laser source (4.64 eV) shows SP around E_F reach for -72%. They also demonstrate that Fe_3O_4 can be described by a band

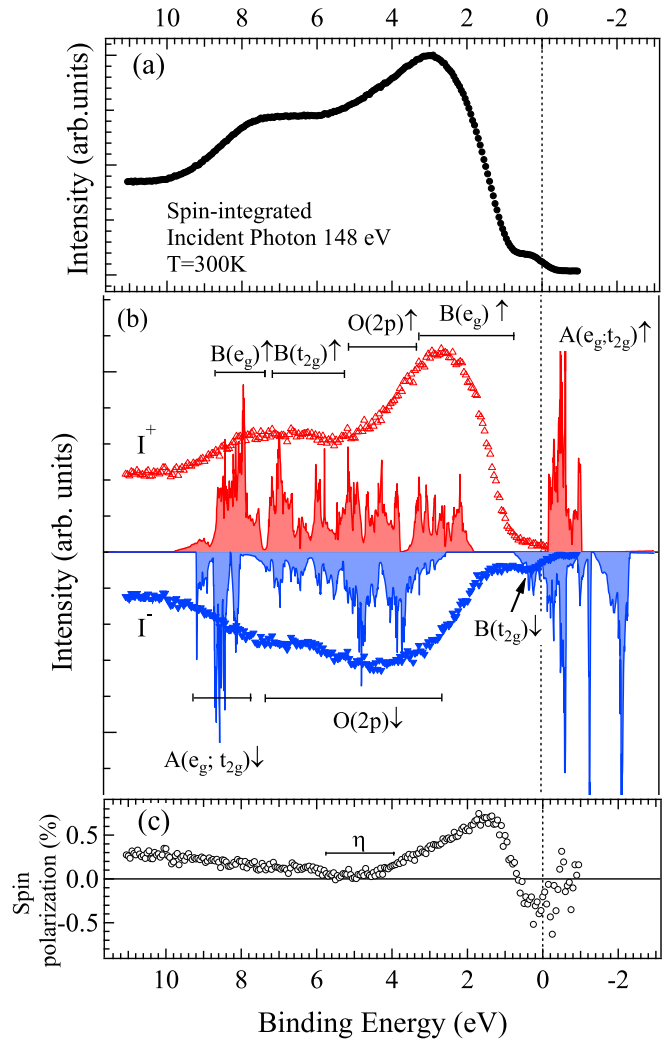

FIG. 9. (a) Soft x-ray spin-integrated and (b) spin-resolved valence band photoemission spectrum of 150-ML Fe_3O_4/MgO(100) at room temperature. (c) Dependence of spin polarization on binding energy. (Experimental data reproduce from Refs. [66–69].)

model and strongly support its half-metallic nature. Apart from emissions near E_F, spin-polarized spectrum was fairly consistent with the GGA $+U$ results, as did the OMCD spectrum. The increase in I^+ (0.5–2.0 eV) exceeded that in I^-, resulting in the dominance of positive SP in $B(e_g)\uparrow$. The SP value peaked at 1.5 eV; subsequently, the value decreased gradually as the entering of minority $2p$ oxygen and reached 0 at 4.5–5.5 eV. These relationships may elucidate the bare electronic states observed through OMCD and SPES.

VII. CONCLUSION

We demonstrated the electron correlation effect plays a crucial role in describing magnetite in terms of magneto-optical properties. The main factors influencing such properties were determined to be the optical gaps of spin majority and spin minority, which can only be reproduced with Hubbard $-U$ correction. GGA $+U$ calculations were performed to determine the electronic structure in the BE range of 2–5.5 eV. The result indicated that dominant states of spin majority

and spin minority are $B(e_g;t_{2g})\uparrow$ and $O(2p)\downarrow$, respectively. Optical charge transfer within magnetite could be classified into three categories: (1) IVCT of spin minority relax from parity selection due to lattice distortion; (2) ISCT mediated by $2p$ oxygen across the optical gap of spin majority; and (3) LMCT across the optical gap of spin minority. We thus conclude that the optical transition of magnetite within the interval 0.5–5 eV exhibits the signature of a Mott insulator. We mapped detailed structures associated with the dominant spin channel of charge transfer in the magnetite thin films. Optical gaps of spin majority and spin minority were determined to be 2.35 and 2.5 eV, respectively. We conclude that the OMCD spectrum of magnetite can generally reflect the optical transition from the B site and manifest the competition between the polarized Fe($3d$) majority and $O(2p)$ minority. The transmitting OMCD spectrum of magnetite was determined to exhibit a similar trend to the valence band spin polarization obtained through Mott polarimetry. Both results reflected the B-site spin states.

In this study, the transmitting OMCD served as a simple laboratory probe for exploring bulk sensitive magnetism originating from spin-split valence electronic structures. The strategy provided in this work permits the in-line inspections for spin-selective charge transfer of magnetic-oxide based heterosystem and possibly probes into the surface reaction as well as emergent phenomena at oxide interfaces.

ACKNOWLEDGMENTS

This work is supported by the Ministry of Science and Technology of Taiwan under Grant No. MOST 106-2112-M-153-003.

[1] J. R. Neal, A. J. Behan, R. M. Ibrahim, H. J. Blythe, M. Ziese, A. M. Fox, and G. A. Gehring, Phys. Rev. Lett. **96**, 197208 (2006).
[2] H. Weng, J. Dong, T. Fukumura, M. Kawasaki, and Y. Kawazoe, Phys. Rev. B **73**, 121201 (2006).
[3] G. A. Gehring, M. S. Alshammari, D. S. Score, J. R. Neal, A. Mokhtari, and A. M. Fox, J. Magn. Magn. Mater. **324**, 3422 (2012).
[4] M. S. Alshammari, M. S. Alqahtani, H. B. Albargi, S. A. Alfihed, Y. A. Alshetwi, A. A. Alghihab, A. M. Alsamrah, N. M. Alshammari, M. A. Aldosari, A. Alyamani, A. M. H. R. Hakimi, S. M. Heald, H. J. Blythe, M. G. Blamire, A. M. Fox, and G. A. Gehring, Phys. Rev. B **90**, 144433 (2014).
[5] H. Yao and Y. Ishikawa, J. Phys. Chem. **119**, 13224 (2015).
[6] E. Fantechi, G. Campo, D. Carta, A. Corrias, C. de Julián Fernández, D. Gatteschi, C. Innocenti, F. Pineider, F. Rugi, and C. Sangregorio, J. Phys. Chem. **116**, 8261 (2012).
[7] M. Imada, A. Fujimori, and Y. Tokura, Rev. Mod. Phys. **70**, 1039 (1998).
[8] N. Tsuda, K. Nasu, A. Fujimori, and K. Shiratori, *Electronic Conduction in Oxides, 2nd ed.* (Springer-Verlag, Berlin, 1994), p. 243.
[9] P. J. van der Zaag, W. F. J. Fontijn, P. Gaspard, R. M. Wolf, V. A. M. Brabers, R. J. M. van de Veerdonk, and P. A. A. van der Heijden, J. Appl. Phys. **79**, 5936 (1996).
[10] W. F. J. Fontijn, P. A. A. van der Heijden, F. C. Voogt, T. Hibma, and P. J. van der Zaag, J. Magn. Magn. Mater. **165**, 401 (1997).
[11] W. F. J. Fontijn, R. M. Wolf, R. Metselaar, and P. J. van der Zaag, Thin Solid Film **292**, 270 (1997).
[12] W. F. J. Fontijn, P. J. van der Zaag, M. A. C. Devillers, V. A. M. Brabers, and R. Metselaar, Phys. Rev. B **56**, 5432 (1997).
[13] W. F. J. Fontijn, P. J. van der Zaag, L. F. Feiner, R. Metselaar, and M. A. C. Devillers, J. Appl. Phys. **85**, 5100 (1999).
[14] E. J. W. Verwey, Nature (London) **144**, 327 (1939); E. J. W. Verwey and P. W. Haayman, Physica (Amsterdam) **8**, 979 (1941).
[15] V. I. Anisimov, I. S. Elfimov, N. Hamada, and K. Terakura, Phys. Rev. B **54**, 4387 (1996).
[16] Z. Zhang and S. Satpathy, Phys. Rev. B **44**, 13319 (1991).
[17] J. P. Wright, J. P. Attfield, and P. G. Radaelli, Phys. Rev. Lett. **87**, 266401 (2001); Phys. Rev. B **66**, 214422 (2002).
[18] H.-T. Jeng, G. Y. Guo, and D. J. Huang, Phys. Rev. Lett. **93**, 156403 (2004).
[19] I. Leonov, A. N. Yaresko, V. N. Antonov, M. A. Korotin, and V. I. Anisimov, Phys. Rev. Lett. **93**, 146404 (2004).
[20] H.-T. Jeng, G. Y. Guo, and D. J. Huang, Phys. Rev. B **74**, 195115 (2006).
[21] I. Leonov, A. N. Yaresko, V. N. Antonov, and V. I. Anisimov, Phys. Rev. B **74**, 165117 (2006).
[22] D. J. Huang, H.-J. Lin, J. Okamoto, K. S. Chao, H.-T. Jeng, G. Y. Guo, C.-H. Hsu, C.-M. Huang, D. C. Ling, W. B. Wu, C. S. Yang, and C. T. Chen, Phys. Rev. Lett. **96**, 096401 (2006).
[23] J. Schlappa, C. Schüßler-Langeheine, C. F. Chang, H. Ott, A. Tanaka, Z. Hu, M. W. Haverkort, E. Schierle, E. Weschke, G. Kaindl, and L. H. Tjeng, Phys. Rev. Lett. **100**, 026406 (2008).
[24] A. Tanaka, C. F. Chang, M. Buchholz, C. Trabant, E. Schierle, J. Schlappa, D. Schmitz, H. Ott, P. Metcalf, L. H. Tjeng, and C. Schüßler-Langeheine, Phys. Rev. Lett. **108**, 227203 (2012).
[25] M. S. Senn, J. P. Wright, and J. P. Attfield, Nature (London) **481**, 173 (2012).
[26] H. Y. Huang, Z. Y. Chen, R.-P.Wang, F. M. F. de Groot, W. B. Wu, J. Okamoto, A. Chainani, A. Singh, Z.-Y. Li, J.-S. Zhou, H.-T. Jeng, G. Guo, J.-G. Park, L. H. Tjeng, C. T. Chen, and D. J. Huang, Nat. Commun. **8**, 15929 (2017).
[27] M. S. Senn, J. P. Wright, J. Cumby, and J. P. Attfield, Phys. Rev. B **92**, 024104 (2015).
[28] M. Taguchi, A. Chainani, S. Ueda, M. Matsunami, Y. Ishida, R. Eguchi, S. Tsuda, Y. Takata, M. Yabashi, K. Tamasaku, Y. Nishino, T. Ishikawa, H. Daimon, S. Todo, H. Tanaka, M. Oura, Y. Senba, H. Ohashi, and S. Shin, Phys. Rev. Lett. **115**, 256405 (2015).
[29] J. Chen, D. J. Huang, A. Tanaka, C. F. Chang, S. C. Chung, W. B. Wu, and C. T. Chen, Phys. Rev. B **69**, 085107 (2004).
[30] J. Garcia, G. Subias, M. G. Proietti, H. Renevier, Y. Joly, J. L. Hodeau, J. Blasco, M. C. Sanchez, and J. F. Berar, Phys. Rev. Lett. **85**, 578 (2000).
[31] J. García and G. Subaís, J. Phys.: Condens. Matter **16**, R145(R) (2004).
[32] J. Zaanen, G. A. Sawatzky, and J. W. Allen, Phys. Rev. Lett. **55**, 418 (1985).

[33] V. I. Anisimov, J. Zaanen, and O. K. Andersen, Phys. Rev. B **44**, 943 (1991).

[34] V. I. Anisimov, I. V. Solovyev, M. A. Korotin, M. T. Czyzyk, and G. A. Sawatzky, Phys. Rev. B **48**, 16929 (1993).

[35] T. Fujii, M. Takano, R. Katano, Y. Bando, and Y. Isozumi, J. Cryst. Growth **99**, 606 (1990).

[36] F. C. Voogt, T. Fujii, P. J. M. Smulders, L. Niesen, M. A. James, and T. Hibma, Phys. Rev. B **60**, 11193 (1999).

[37] J. M. Gaines, J. T. Kohlhepp, P. J. H. Bloemen, R. M. Wolf, A. Reinders, and R. M. Jungblut, J. Magn. Magn. Mater **165**, 439 (1997).

[38] J. M. Gaines, P. J. H. Bloemen, J. T. Kohlhepp, C. W. T. Bulle-Lieuwma, R. M. Wolf, A. Reinders, R. M. Jungblut, P. A. A. van der Heijden, J. T. W. M. van Eemeren, J. aan de Stegge, and W. J. M. de Jonge, Surf. Sci. **373**, 85 (1997).

[39] Y. Gao and S. A. Chambers, J. Cryst. Growth **174**, 446 (1997).

[40] Y. Gao, Y. J. Kim, S. A. Chambers, and G. Bai, J. Vac. Sci. Technol. A **15**, 332 (1997).

[41] Y. J. Kim, Y. Gao, and S. A. Chambers, Surf. Sci. **371**, 358 (1997).

[42] C. F. Chang, Z. Hu, S. Klein, X. H. Liu, R. Sutarto, A. Tanaka, J. C. Cezar, N. B. Brookes, H.-J. Lin, H. H. Hsieh, C. T. Chen, A. D. Rata, and L. H. Tjeng, Phys. Rev. X **6**, 041011 (2016).

[43] R. Aragón, D. J. Buttrey, J. P. Shepherd, and J. M. Honig, Phys. Rev. B **31**, 430 (1985).

[44] J. P. Shepherd, J. W. Koenitzer, R. Aragón, J. Spałek, and J. M. Honig, Phys. Rev. B **43**, 8461 (1991).

[45] D. T. Margulies, F. T. Parker, F. E. Spada, R. S. Goldman, J. Li, R. Sinclair, and A. E. Berkowitz, Phys. Rev. B **53**, 9175 (1996).

[46] D. T. Margulies, F. T. Parker, M. L. Rudee, F. E. Spada, J. N. Chapman, P. R. Aitchison, and A. E. Berkowitz, Phys. Rev. Lett. **79**, 5162 (1997).

[47] F. C. Voogt, T. T. M. Palstra, L. Niesen, O. C. Rogojanu, M. A. James, and T. Hibma, Phys. Rev. B **57**, R8107(R) (1998).

[48] T. Hibma, F. C. Voogt, L. Niesen, P. A. A. van der Heijden, W. J. M. de Jonge, J. J. T. M. Donkers, and P. J. van der Zaag, J. Appl. Phys. **85**, 5291 (1999).

[49] W. Eerenstein, T. T. M. Palstra, S. S. Saxena, and T. Hibma, Phys. Rev. Lett. **88**, 247204 (2002).

[50] J. P. Perdew, K. Burke, and M. Ernzerhof, Phys. Rev. Lett. **77**, 3865 (1996).

[51] G. Kresse and J. Hafner, Phys. Rev. B **47**, 558 (1993).

[52] H. C. Hamilton, Phys. Rev. **110**, 1050 (1958).

[53] S. L. Dudarev, G. A. Botton, S. Y. Savrasov, C. J. Humphreys, and A. P. Sutton, Phys. Rev. B **57**, 1505 (1998).

[54] H.-T. Jeng and G. Y. Guo, Phys. Rev. B **65**, 094429 (2002).

[55] W. Wang, J.-M. Mariot, M. C. Richter, O. Heckmann, W. Ndiaye, P. DePadova, A. Taleb-Ibrahimi, P. LeFèvre, F. Bertran, F. Bondino, E. Magnano, J. Krempaský, P. Blaha, C. Cacho, F. Parmigiani, and K. Hricovini, Phys. Rev. B **87**, 085118 (2013).

[56] A. Chainani, T. Yokoya, T. Morimoto, T. Takahashi, and S. Todo, Phys. Rev. B **51**, 17976 (1995).

[57] V. N. Antonov, B. N. Harmon, V. P. Antropov, A. Y. Perlov, and A. N. Yaresko, Phys. Rev. B **64**, 134410 (2001).

[58] C. J. Ballhausen, *Introduction to Ligand Filed Theory* (McGraw-Hill Book Company, Inc., New York, San Francisco, 1962), p. 103.

[59] S. K. Park, T. Ishikawa, and Y. Tokura, Phys. Rev. B **58**, 3717 (1998).

[60] K. J. Kim, H. S. Lee, M. H. Lee, and S. H. Lee, J. Appl. Phys. **91**, 9974 (2002).

[61] D. L. Camphausen, J. M. D. Coey, and B. K. Chakraverty, Phys. Rev. Lett. **29**, 657 (1972).

[62] J.-H. Park, L. H. Tjeng, J. W. Allen, P. Metcalf, and C. T. Chen, Phys. Rev. B **55**, 12813 (1997).

[63] W. Reim and J. Schoenes, in *Handbook of Ferromagnetic Material*, edited by E. Wohlfarth and K. Buschow (North-Holland, Amsterdam, 1990), Vol. 5, Chap. 2, p. 136.

[64] R. Pentcheva, F. Wendler, H. L. Meyerheim, W. Moritz, N. Jedrecy, and M. Scheffler, Phys. Rev. Lett. **94**, 126101 (2005).

[65] M. Fonin, R. Pentcheva, Y. S. Dedkov, M. Sperlich, D. V. Vyalikh, M. Scheffler, U. Rüdiger, and G. Güntherodt, Phys. Rev. B **72**, 104436 (2005).

[66] J. Chen, *Influence of Electronic Correlations on the Electronic Structure of Half-Metallic Oxide*, Ph.D. thesis, National Chung Cheng University, Taiwan (2003).

[67] D. J. Huang, W. P. Wu, J. Chen, C. F. Chang, S. C. Chung, M. Yuri, H. J. Lin, P. D. Johnson, and C. T. Chen, Rev. Sci. Instrum. **73**, 3778 (2002).

[68] D. J. Huang, C. F. Chang, J. Chen, L. H. Tjeng, A. D. Rata, W. P. Wu, S. C. Chung, H. J. Lin, T. Hibma, and C. T. Chen, J. Magn. Magn. Mater. **239**, 261 (2002).

[69] D. J. Huang, C. F. Chang, J. Chen, L. H. Tjeng, A. D. Rata, W. P. Wu, S. C. Chung, H. J. Lin, T. Hibma, and C. T. Chen, Surf. Rev. Lett. **9**, 1007 (2002).

[70] F. B. Dunning, Nucl. Instrum. Methods Phys. Res., Sect. A **347**, 152 (1994).

[71] S. F. Alvarado, W. Eib, F. Meier, D. Pierce, K. Sattler, and H. C. Siegmann, Phys. Rev. Lett. **34**, 319 (1975); S. F. Alvarado, M. Erbudak, and P. Munz, Phys. Rev. B **14**, 2740 (1976); S. F. Alvarado and P. S. Bagus, Phys. Lett. A **67**, 397 (1978).

[72] S. A. Morton, G. D. Waddill, S. Kim, I. K. Schuller, S. A. Chambers, and J. G. Tobin, Surf. Sci. **513**, L451 (2002).

[73] E. Vescovo, H.-J. Kim, J. M. Ablett, and S. A. Chambers, J. Appl. Phys. **98**, 084507 (2005).

[74] J. G. Tobin, S. A. Morton, S. W. Yu, G. D. Waddill, I. K. Schuller, and S. A. Chambers, J. Phys.: Condens. Matter **22**, 315218 (2007).